Electrochemical exsolution of metal nanoparticles from perovskite oxide upon electrolysis

Jaesung Kim [a], Seval Gunduz [a], Anne C. Co [b], Umit S. Ozkan [a],*

[a] *William G. Lowrie Department of Chemical and Biomolecular Engineering, The Ohio State University, Columbus, OH 43210, United States*
[b] *Department of Chemistry and Biochemistry, The Ohio State University, Columbus, OH 43210, United States*

ARTICLE INFO

ABSTRACT

This study presents a comprehensive investigation into the electrochemical reduction of LSCF perovskite during electrolysis, aiming to understand the exsolution of metal nanoparticles. The exsolution of metal nanoparticles from perovskite electrodes can significantly enhance their electrochemical performance in electrolysis. By applying cathodic polarization to the perovskite oxide electrode, the exsolution process was shown to be electrochemically induced within a few minutes. Additionally, a user-designed X-ray absorption spectroscopy *operando* cell was employed to analyze the edge energy change of the B-site atoms during electrolysis. The electrochemical reduction of perovskite and the subsequent exsolution of the B-site metal nanoparticles were investigated by scanning the cell voltage, providing an understanding of the electrochemical behavior during electrolysis. The electrochemical switching point, characterized by a decrease in the incremental area-specific resistance, was identified. This study offers valuable insights into the electrochemical exsolution process of metal nanoparticles from perovskite oxide electrodes.

1. Introduction

ABO$_3$ perovskite oxides are widely used for energy and chemical conversion processes as mixed ionic and electronic conductors (MIECs) in solid oxide electrocatalytic cells. These materials have garnered significant attention in the scientific community due to their exceptional redox properties, which are linked to their tunable oxygen ion mobility, high stability under both oxidizing and reducing environments, and resistance to coke formation [1–4]. To improve the electronic and ionic conductivity, stability, or activity of these materials, many studies have focused on doping the A or B sites of perovskite oxides.

It has been proven that a controlled reducing environment at elevated temperatures may be used to induce the exsolution of B-site atoms onto the surface [5–13]. During thermochemical exsolution, B-site transition metal atoms undergo reduction and migrate towards the surface, where they segregate into nanoparticles. By contrast to the physical deposition techniques, exsolution results in the formation of well-distributed and uniform sized nanoparticles that adhere firmly to the parent perovskite surface with superior thermochemical stability [14–17].

It is noteworthy that exsolution of metal nanoparticles can be triggered by applying cathodic polarization to the perovskite oxide electrode. It has been also reported that the electrochemical exsolution could be induced by anodic polarization due to incomplete oxidation and local charge transfer [18–20]. The electrochemical exsolution is time efficient given that it can be achieved within several minutes by applying polarization. This is why the electrochemical exsolution is referred to as "electrochemical switching" [19]. In contrast, the thermal exsolution under reducing atmosphere normally requires several hours of treatment due to the slow diffusion and low driving force ($\propto (k_B T)/2 \ln P_{H2}$) [21]. However, studies on the electrochemical exsolution are limited so far because the process requires high temperature, electrical lead connections, controlled gas environment, which make in-situ and ex-situ observation difficult.

The goal of the present work is to provide insights into the electrochemical reduction of the working electrode and the resultant exsolution during the electrolysis process. The electrochemical switching point was presented with area-specific resistance by scanning the cell voltage. X-ray absorption spectroscopy data was obtained to evaluate the elemental edge energy during electrolysis using a user-designed *operando* cell.
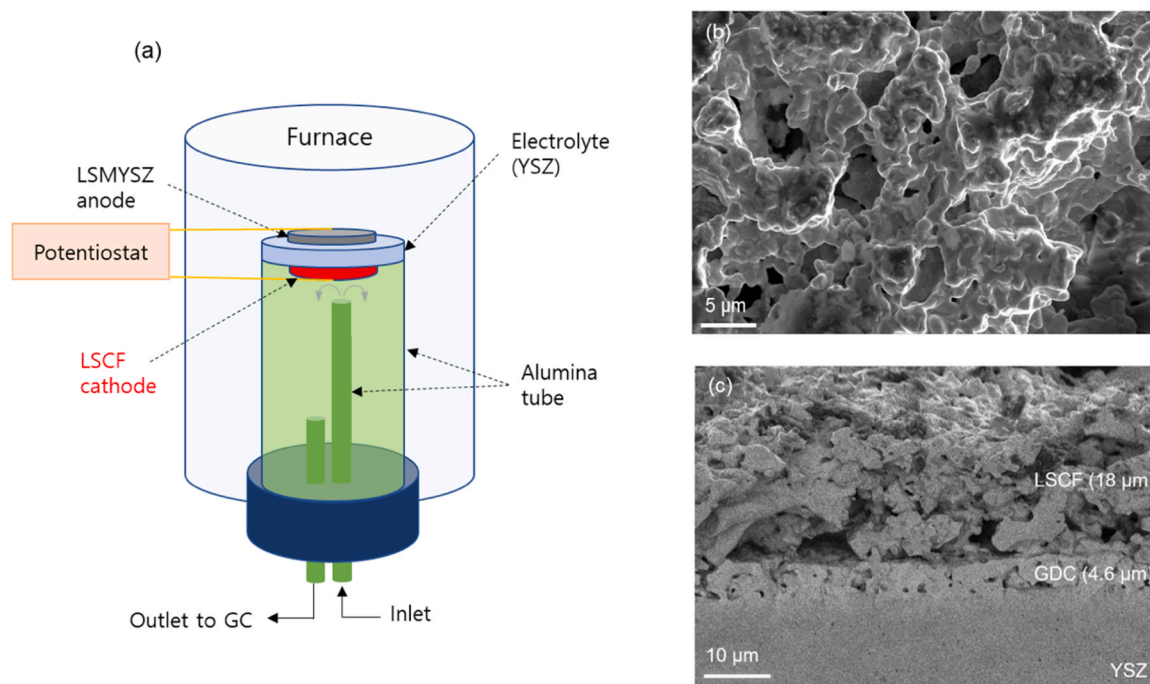
Fig. 1. (a) Schematic illustration of the electrocatalytic reaction system. SEM images of LSCF cathode (a) top surface (secondary electron) and (b) cross-section (backscattered electron).

2. Experimental

2.1. Preparation of catalysts

$La_{0.7}Sr_{0.2}Co_{0.2}Fe_{0.8}O_3$ (LSCF) perovskite, as reported in our earlier publications, was synthesized by a citric acid-ethylenediaminetetraacetic acid complexation method [22]. A mixture of metal-nitrate salts dissolved in a stoichiometric amount in 100 ml of deionized water. Ethylenediaminetetraacetic acid was added to the solution with a 1:1 molar ratio to the total metal ions. Ammonium hydroxide was also added to the solution to stabilize pH at 6 at 60 °C. After adding ethylene glycol and citric acid, the solution was heated to 90 °C while maintaining pH of 6. After evaporation, the gel formed was dried at 150 °C overnight. The dried black powder was calcined at 1000 °C for 5 h to produce crystalline LSCF.

2.2. Catalyst characterization

X-ray diffraction patterns were acquired using a Bruker D8 Lead X-ray powder diffractometer equipped with a Cu Kα X-ray source. The voltage and current in the generator were 40 kV and 40 mA, respectively. Scans were conducted with a 2θ range from 20° to 60°, and the step size was set at 0.019° per 0.5 s. Crystallographic open database (COD) was used to identify phases [23]. Miller indices were calculated from the XRD patterns by Rietveld refinement method using General Structure Analysis System-2 (GSAS-2) software [24]. In-situ XRD was performed with an Anton Paar HTK1200 oven at temperature ranges of 30 °C to 800 °C.

Operando X-ray Absorption Near Edge Spectroscopy (XANES) was carried out in fluorescence mode at Sector 10-ID of the Materials Research Collaborative Access Team (MRCAT) at the Advanced Photon Source (APS, Argonne National Laboratory). Detailed information about the user-made *operando* cell design can be found in our previous study [25]. The button cell was located at the center of the F-factor at 45° angle to the incident X-ray beam. The inlet stream was 50 ccm of 3% H_2O/N_2 at 650 °C. The current was applied using Keithley 6220. The collected XANES data was processed using Athena software [26].

The visual examination of the nanoparticles was conducted using a scanning transmission electron microscope (STEM), a TECNAI F20 equipped with an energy dispersive X-ray spectrometer (EDS). Scanning electron microscope images (SEM) were taken using FEI Apreo instrument with an EDS. SEM images of the LSCF cathode after cathodic polarization were captured to examine the surface of LSCF. The reactor was filled with helium during the cooling process.

Diffuse reflectance infrared Fourier transform spectroscopy (DRIFTS) data was acquired using Thermoelectron Nicolet 6700 FTIR. In a 1:20 ratio, powder samples were diluted with potassium bromide (KBr). The samples were pretreated with He at 450 °C prior to temperature-programmed desorption (TPD) -DRIFTS in order to desorb any additional adsorbate. DRIFTS spectra were collected under He at various temperatures after CO_2 or H_2O exposure at 50 °C.

The electrical conductivity of the catalyst samples was evaluated using pellets that were prepared by compressing the powder using a hydraulic press, followed by sintering at 1300 °C for 5 h. Four gold wires were affixed to the pellet using gold paste at four designated points. A Keithley 6220 current source was connected to two of the wires to provide current, while a Keithley 6182 sensitive nanovoltmeter was connected to the other two wires to measure the resulting voltages. In-situ measurement was performed under 50 ccm of 5% H_2/He atmosphere.

2.3. Evaluation of electrocatalytic performance

The electrochemical button cells were made by screen-printing on commercial yttria-stabilized zirconia (YSZ) electrolyte (25 mm diameter, 125 μm thickness, Nextech Materials). The cathode side was coated with gadolinium-doped ceria (GDC) interlayer that was sintered under air at 1400 °C for 2 h. LSCF powder was printed with a 0.28 cm^2 surface area on the GDC interlayer and sintered at 1200 °C under air for 2 h. A mixture of $(La_{0.80}Sr_{0.20})_{0.95}MnO_3$- $(Y_2O_3)_{0.08}(ZrO_2)_{0.92}$ (LSM-YSZ; Nextech Materials) in a weight ratio of 1 to 1 was screen-printed on the anode side and sintered at 1200 °C under air for 2 h. A gold wire and platinum paste were used to attach the gold mesh to the electrodes. A total flow rate of 60 ccm was used for the electrocatalytic performance
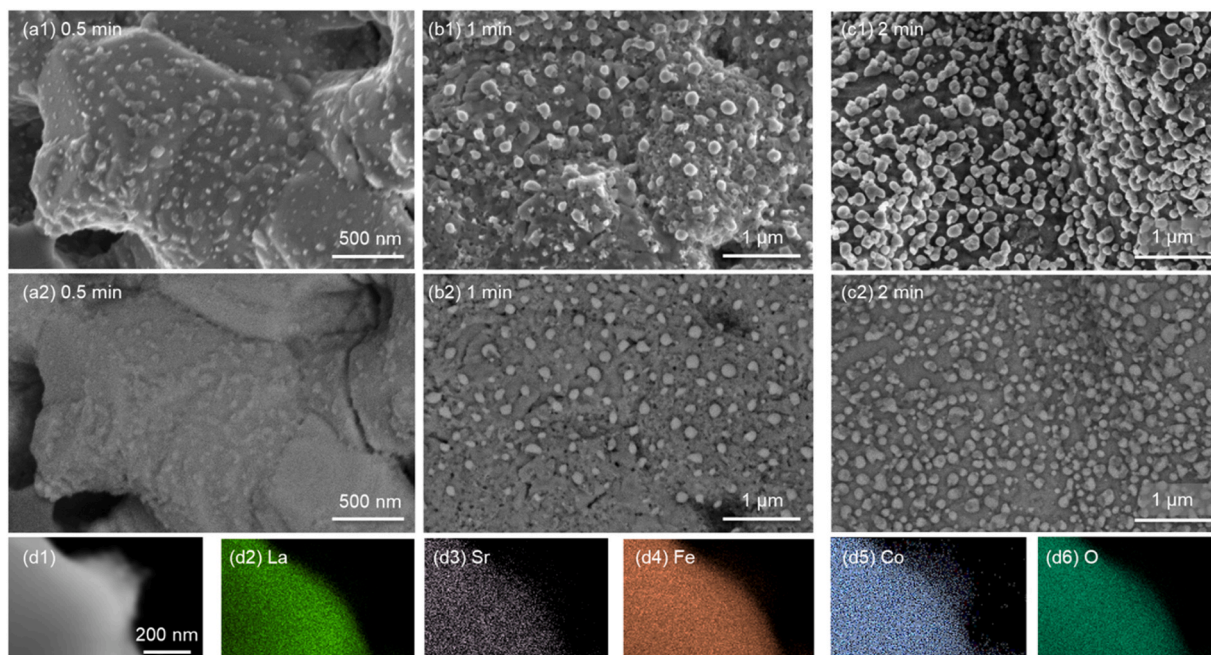
Fig. 2. SEM secondary electron (1) and backscattered electron (2) images of LSCF cathode after applying − 1.3 V of cathodic potential under helium at 700 °C for (a1,a2) 0.5 min, (b1,b2) 1 min, and (c1,c2) 2 min, (d1) STEM image of the electrochemically exsolved nanoparticle with elemental mapping of (d2) La, (d3) Sr, (d4) Fe, (d5) Co, and (d6) O after 2 min of − 1.3 V cathodic polarization at 700 °C.

test with a feed gas concentration of 5% H_2O, 5% CO_2, and balanced He at the cathode. Electrochemical impedance spectra (EIS) were collected within the frequency range of 1 MHz to 10 mHz. The current was scanned by increasing the cell voltage from 0 to –2 V at different scan rates ranging 0.1–100 mV s^{-1}. The equivalent circuit model of $R_S(R_{P1}Q_1)$ $(R_{P2}Q_2)$ was used, which is composed of an ohmic resistance R_S and two polarization resistances (R_P) and constant phase elements (Q) in parallel. Gas products were quantified with an on-line gas chromatograph (Shimadzu 2014) equipped with a pulse discharge helium ionization detector (PDHID).

3. Results and discussion

3.1. Electrochemical reduction of LSCF

The structural analysis of the synthesized $La_{0.7}Sr_{0.2}Co_{0.2}Fe_{0.8}O_3$ (LSCF) power is presented in Fig. S1. Electrochemical reduction of the LSCF perovskite and co-electrolysis of H_2O and CO_2 were conducted in the experimental setup depicted in Fig. 1(a). The top surface and cross-section images of the LSCF button cell are shown in Fig. 1(b,c). The LSCF cathode was well densified to provide ionic and electrical conductivity while also having enough porosity to facilitate the transport of reactants. The gadolinium-doped ceria (GDC) layer, which has a thickness of 4.6 μm, was placed between the LSCF cathode and YSZ electrolyte to prevent any reaction between the two materials.

In order to isolate the effect of cathodic polarization from gas phase oxidation/reduction, the electrochemical reduction of the LSCF electrode was conducted under helium at 700 °C. As no gas phase reactant was reduced by the applied current, the electrons were assumed to participate in reducing the lattice oxygen within the LSCF perovskite electrode. Scanning electron microscope (SEM) images in Fig. 2(a,b,c) illustrate the top surface of the LSCF electrode after applying a cathodic potential of –1.3 V for 0.5–2 min. Nanoparticles were found in secondary electron SEM image even after 0.5 min of polarization (Fig. 2(a1)). The backscattered electron SEM image (Fig. 2(a2)) revealed compositional differences between the exsolved nanoparticles and the parent perovskite. Over time, the nanoparticles grew in size and exhibited

uniformity, covering the entire perovskite surface after 2 min of potential application. In Fig. 2(d), the Scanning Transmission Electron Microscope (STEM) image and corresponding elemental mapping for different elements are presented. Fig. 2(d1) shows the STEM image of an exsolved metal nanoparticle, protruding to the right from the bulk, a result of subjecting the sample to a cathodic polarization of –1.3 V at 700 °C for 2 min. In Fig. 2(d2, d3, d4, d5, d6), the elemental mapping of lanthanum (La), strontium (Sr), iron (Fe), cobalt (Co), and oxygen (O), respectively, are presented. The figures clearly illustrate that cobalt is the sole element detected on the exsolved nanoparticle, signifying the presence of pure cobalt metal. This result unequivocally confirms the selective exsolution of cobalt nanoparticles on the LSCF surface.

Fig. S2 provides further confirmation of exsolved nanoparticles on the surface of LSCF perovskite, as verified through Scanning Electron Microscopy (SEM) coupled with Energy-Dispersive X-ray Spectroscopy (EDS). The exsolved nanoparticles emerged following a cathodic polarization of –1.3 V at 700 °C for 2 min. Notably, the elemental mapping reveals decreased counts of O, Fe, and La on the nanoparticles, while Co remains present on the particle surface. This observation strongly supports the phenomenon of selective exsolution of cobalt nanoparticles on the LSCF perovskite surface. The exsolution of CoFe bimetallic nanoparticles investigated in our previous study required a high temperature (850 °C), reducing environment (5% H_2/N_2), and long duration time (3 h) to acquire the similar size of nanoparticles with this study [27]. Notably, the fast process of electrochemical reduction relies on charge transfer throughout the perovskite structure, contrasting with the slow diffusion of metal atoms and relatively low driving force ($\propto (k_BT)/2$ ln P_{H2}) for thermochemical exsolution [21]. This process can be understood through the following expressions based on Kröger–Vink notation:

Thermochemical exsolution

$$B_B^X + \frac{m}{2}O_O^X + \frac{m}{2}H_2 \leftrightarrow V_B^{m'} + \frac{m}{2}V_O^{\bullet\bullet} + B_{surface} + \frac{m}{2}H_2O(g) \qquad (1)$$

Electrochemical exsolution

$$B_B^X + \frac{m}{2}O_O^X + me^- \leftrightarrow V_B^{m'} + \frac{m}{2}V_O^{\bullet\bullet} + B_{surface} + \frac{m}{2}O^{2-} \qquad (2)$$

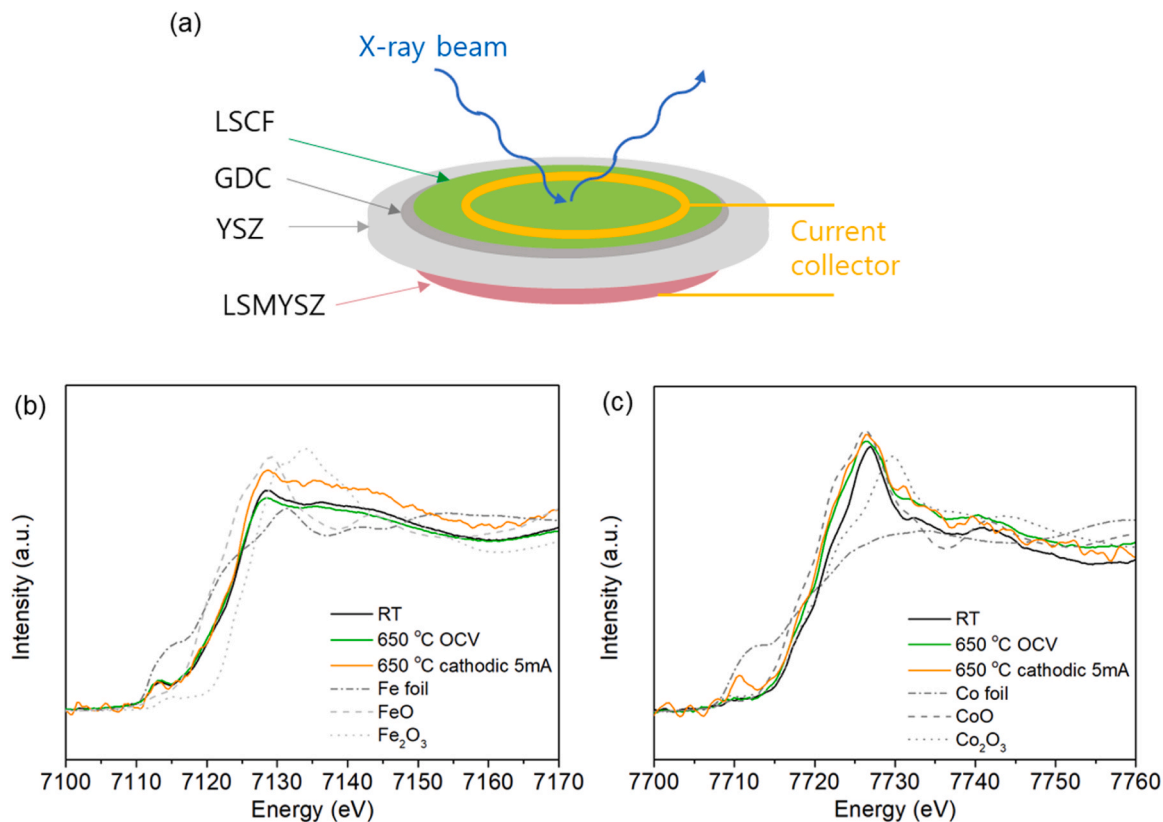where B_B^X indicates a transition metal occupying the B-site of the

Fig. 3. (a) Illustration of the *operando* XANES analysis on LSCF electrode at 45° angle to the incident X-ray beam. The *operando* XANES results on (b) Fe K edge and (c) Co K edge at room temperature, 650 °C under open-circuit voltage, and under - 5 mA of cathodic current.
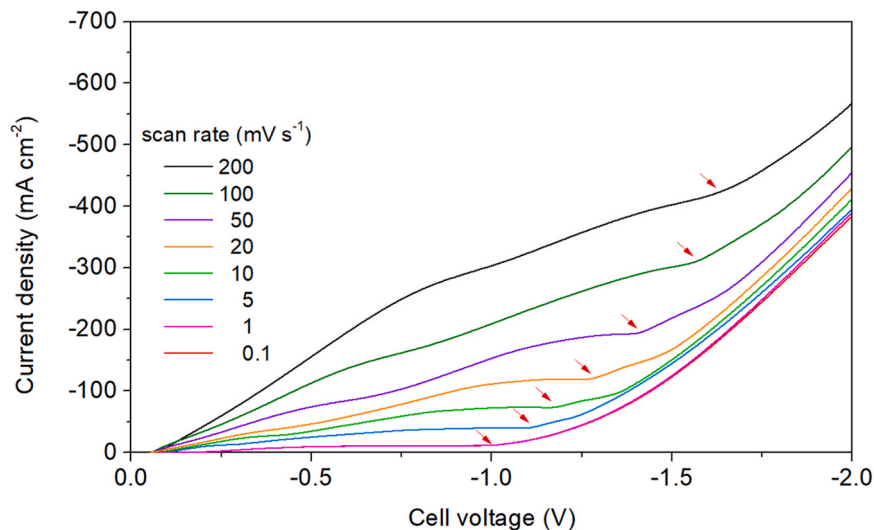

Fig. 4. Current density as a function of cell voltage at different scan rates at 700 °C under 60 ccm of 5% H_2O-5% CO_2.

perovskite lattice, O_O^X denotes a lattice oxygen in the perovskite structure, $V_B^{m'}$ denotes a B-site vacancy, $V_O^{••}$ denotes an oxygen vacancy, and $B_{surface}$ denotes exsolved transition metal.

Applied electrons directly result in the lattice oxygen being ionized and oxygen vacancy being formed and eventually, the B-site transition metal being reduced. The electrochemical exsolution of metal nanoparticles proved to be more efficient than thermochemical reduction. Additionally, this study reveals that the exsolved metal nanoparticles obtained here are larger than those reported in the literature. For instance, Ni nanoparticles exsolved from $La_{0.43}Ca_{0.37}Ni_{0.06}Ti_{0.94}O_{3-γ}$

measured 15 nm after applying 2 V of cathodic polarization for 150 s at 900 °C, while exsolved Ni nanoparticles from $La_{0.4}Ca_{0.4}Ti_{0.88}Fe_{0.06}Ni_{0.06}O_{3-δ}$ ranged from 15 to 42 nm after applying 5 V of cathodic or anodic bipolar shock at 800 °C [18,19]. The considerable size of the exsolved particles (30–200 nm) observed in this study can be attributed to the 10% A-site deficient stoichiometry of the $La_{0.7}Sr_{0.2}Co_{0.2}Fe_{0.8}O_3$ perovskite and the B-site being doped 20% cobalt.
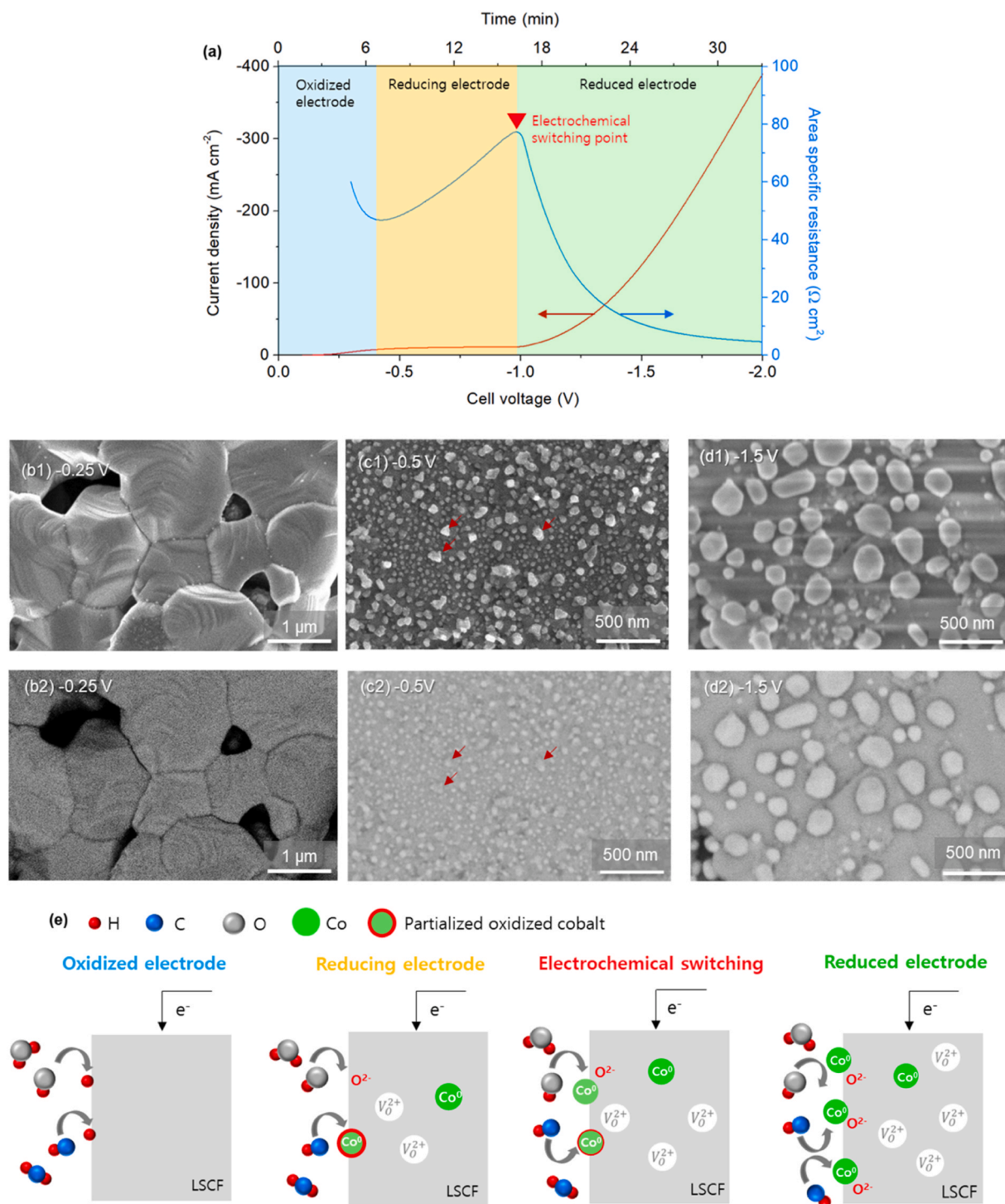
Fig. 5. (a) Current density and the resulting area specific resistance as a function of cell voltage at a scan rate of 1 mV s^{-1}, SEM (b1,c1,c2) secondary electron and (b2, c2,e2) backscattered electron images of LSCF electrode after cathodic polarization at different cell voltages under the co-electrolysis condition for 10 min, (e) schematic illustration of the electrochemical behavior of LSCF electrode at different cell voltages.

3.2. Operando XANES analysis

An *operando* characterization of the LSCF electrode under the electrochemical reaction conditions was conducted to investigate the oxidation state of Co and Fe atoms. The experimental setup utilized a user-designed *operando* cell, as previously reported, connected to a button cell with a ring-shaped current collector [25]. This arrangement allows for the central area of the electrode to be exposed to the incident X-ray beam at a 45-degree angle, as depicted in Fig. 3(a). The *operando*

X-ray absorption near-edge structure (XANES) measurements were carried out in 3% H_2O/N_2. Notably, the Co K-edge energy on the LSCF electrode exhibited a shift to lower values as the temperature increased from room temperature to 650 °C, while the Fe K-edge energy remained unchanged. The absence of pre-edge features associated with metallic Fe and Co atoms in the XANES indicated that these atoms maintained their oxidized forms under open-circuit voltage conditions at elevated temperatures. The Fe XANES showed no significant changes following the application of a 5 mA cathodic current. In contrast, the Co XANES
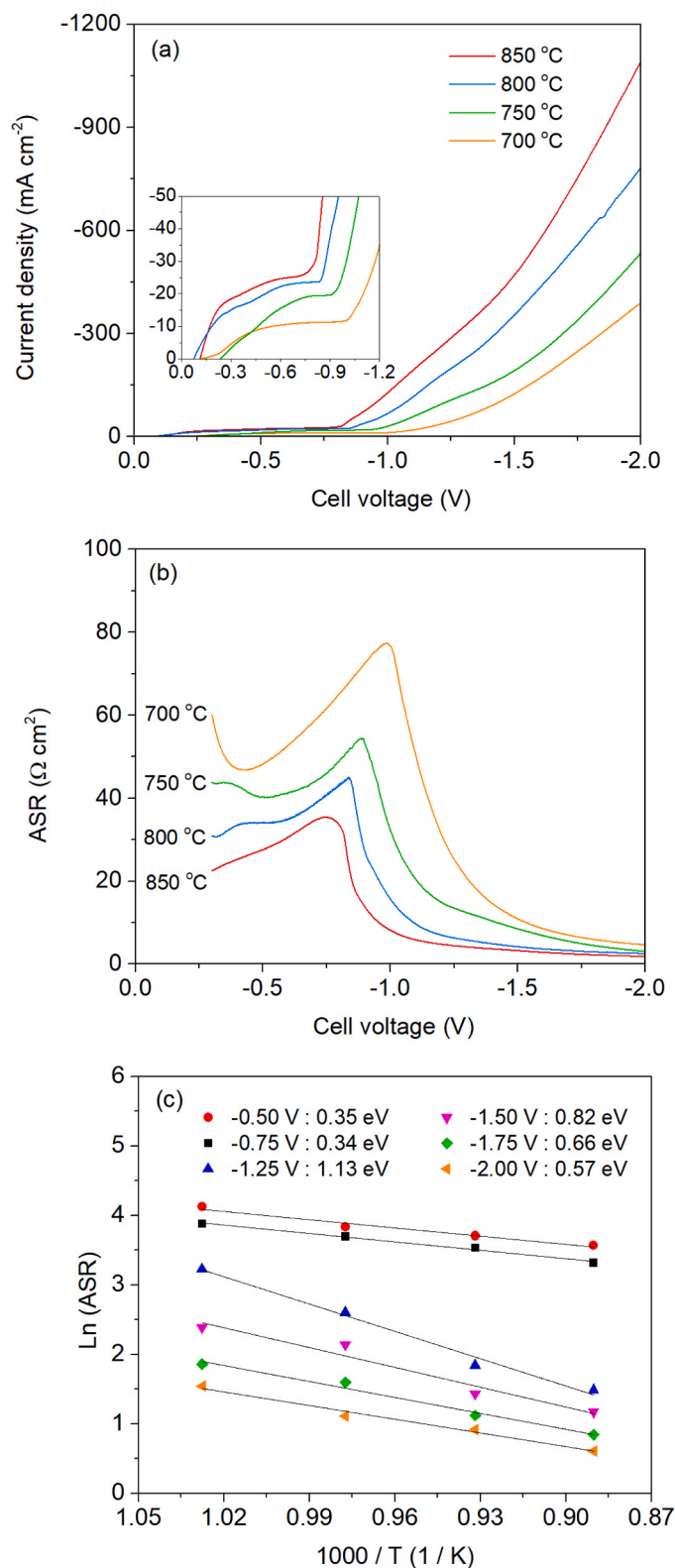
Fig. 6. (a) Current density as a function of cell voltage for co-electrolysis of H_2O and CO_2 at a scan rate of 1 mV s^{-1} at different temperatures and (b) the corresponding ASR, (c) Arrhenius plots of ASR at different cell voltages as a function of temperature.

displayed a shift to lower energy and revealed the appearance of pre-edge features associated with metallic cobalt. This result is consistent with the observations from STEM image with elemental mapping presented in Fig. 2(d). The accurate edge energy calculation for the XANES was challenging due to noise caused by the applied current. Considering that the penetration depth of the incident X-ray beam is approximately 5 μm for Fe and Co atoms with edge energies of 7112 eV and 7717 eV, respectively, these findings suggest that the electrochemical reduction of Co atoms on the LSCF cathode is not limited to the surface but also occurs within the bulk, aligning with previous literature results [18]. It is noteworthy that although the current collector was attached only to the perimeter of the LSCF electrode in a ring shape, electrochemical reduction was observed even in regions where direct contact with the current collector was absent. This observation implies that electrochemical reduction of LSCF may occur throughout the entire electrode.

3.3. Electrochemical behavior during electrolysis

The electrochemical reduction of the LSCF electrode and the resulting exsolution can be influenced by the presence of oxidant gases such as H_2O or CO_2 during electrolysis. This is due to the potential re-oxidation of the reduced LSCF and the exsolved metal nanoparticles. To investigate the electrochemical behavior of the LSCF cell under electrolysis conditions (5% H_2O, 5% CO_2, and balanced He), an analysis of the relationship between cell voltage and current density was conducted.

The measurement of current density was performed by increasing the cell voltage at various scan rates ranging from 0.1 to 200 mV s^{-1}. Fig. 4 shows that higher current densities are observed at faster scan rates, as expected. Another important observation from the polarization curves is the fact that at each scan rate, there is an inflection point, i.e., a point where the slope changes. This point may represent electrochemical reduction of the LSCF and the progression of the exsolution. This finding suggests that the exsolution of metal particles likely takes place at specific voltage values, thereby influencing the electrochemical behavior of the cell. Such electrochemical behavior has been reported as an activation process of the electrode in the literature [28].

To provide a detailed explanation of the electrochemical behavior, the area-specific resistance (ASR) was derived from the I-V curve at 700 °C and a scan rate of 1 mV s^{-1}, as shown in Fig. 5(a). The ASR showed a decline, an increase, and a subsequent decline, which can be explained by dividing the process into three intervals accordingly.

At lower cell voltage (blue area in Fig. 5(a)), the LSCF electrode is likely in a fully oxidized form. At this point, the current density is low and ASR is high. The slight decrease in the ASR with current density is because of the decrease in polarization resistance due to increased voltage. The reduction of H_2O and/or CO_2 occurs at a faster rate compared to the supply of electrons. This suggests that the oxidation of the LSCF electrode by oxidants is faster than its reduction by the supplied electrons. SEM images of the LSCF electrode reveal a clean surface without any exsolved nanoparticles after applying a polarization of –0.25 V for 10 min under electrolysis conditions (Fig. 5(b)). Thus, the LSCF electrode maintains a fully oxidized state as depicted in Fig. 5(e).

In the region shown in yellow, the LSCF electrode undergoes reduction due to the applied electrons. It is noteworthy that despite an increase in cell voltage, the current density does not increase during this stage, while the ASR substantially increases up to 77.6 Ω cm^2. This increase in ASR can be attributed to the decreased electrical conductivity of the LSCF electrode. LSCF perovskite is a p-type electric conductor with charge carriers consisting of $Fe^{2+/3+/4+}$ and $Co^{3+/4+}$ ion pairs [27]. When the supply of electrons exceeds the reduction of H_2O or CO_2, the surplus electrons begin to reduce the lattice oxygen and cobalt in the LSCF perovskite electrode. Then, the concentration of charge carriers decreases and consequently electrical conductivity of LSCF perovskite reduces, resulting in an increased ASR. The electrical conductivity of the electrochemically reduced LSCF is challenging to measure; however, the
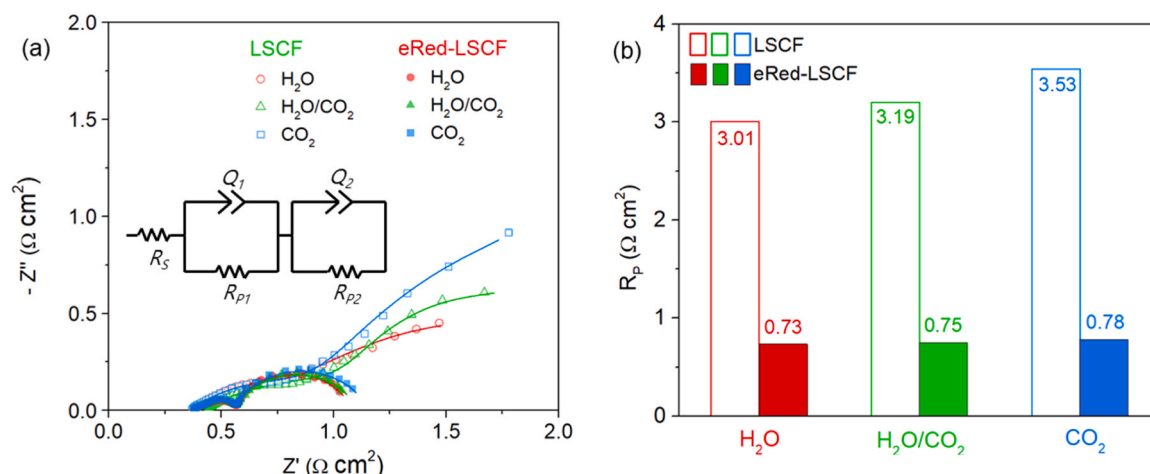
Fig. 7. (a) Electrochemical impedance spectra and (b) the resultant polarization resistance of LSCF and eRed-LSCF at 850 $^\circ$C for H_2O, CO_2, and H_2O/CO_2 electrolysis. Impedance spectra was fitted using the equivalent circuit in (a). eRed-LSCF was prepared by applying –2.0 V of cathodic polarization for 2 min at 850 $^\circ$C.

conductivity of the thermochemically reduced LSCF was measured and found to decrease from 161.1 S cm^{-1} under oxidizing atmosphere to 4.5 S cm^{-1} under 5% H_2/N_2 atmosphere at 850 $^\circ$C (Fig. S3(a)). SEM images reveal the presence of exsolved metal nanoparticles on the LSCF electrode after cathodic polarization of –0.5 V for 10 min through secondary and backscattered electron images in Fig. 5(c). These nanoparticles are predominantly small, and the distinction in brightness between the nanoparticles and the parent LSCF perovskite is not distinctive at certain points, particularly in larger particles, as indicated by the red arrows, even in the presence of helium as a protective gas during the cooling process. This observation suggests that the exsolved nanoparticles may undergo oxidation by H_2O and/or CO_2 on the electrode surface as depicted in Fig. 5(e), which explains the increase in the ASR despite the presence of exsolved nanoparticles during this stage.

The electrochemical switching point is identified as the point (–0.98 V) where the trend of increasing ASR reverses and starts to a decrease, as shown in Fig. 5(a). At this point, the supply of electrons surpasses the oxidation of LSCF and exsolved cobalt nanoparticles by H_2O and/or CO_2. Consequently, exsolved nanoparticles begin to maintain their metallic form against oxidation by H_2O or CO_2 as shown in Fig. 5(e).

In the third region in Fig. 5(a) shown in green, the LSCF electrode is in a fully reduced state, when the cell voltage is above –0.98 V, with numerous exsolved metal nanoparticles, which improve the electrical conductivity of the electrode. At this stage, the electron supply is faster than the reduction of H_2O and CO_2. As a result, oxygen from the reduction of H_2O and CO_2 instantaneously converts into oxygen ions rather than oxidizes the exsolved cobalt nanoparticles or the LSCF perovskite, as illustrated in Fig. 5(e). SEM secondary and backscattered electron images in Fig. 5(d) display large metal nanoparticles (~200 nm) with distinct brightness. The LSCF perovskite electrode becomes decorated with abundant metal nanoparticles that provide metallic conductivity. The electrical conductivity of the thermochemically reduced LSCF as a function of temperature is shown in Fig. S3(b), with the negative slope indicating metallic conductivity. The cobalt nanoparticles, exhibiting conductivity two orders of magnitude greater than LSCF, exsolved on the LSCF surface may augment the electrode's conductivity, thereby leading to a reduction in the ASR [29]. The substantial size and the sustained metallic state of the exsolved Co particles are the key factors in enhancing the ASR during the reduced stage, a stark contrast to the reducing stage. This outcome contrasts with the observed decrease in the electrical conductivity of the thermochemically reduced LSCF perovskite. To examine the difference between electrochemical and thermochemical reduction, a SEM image of LSCF perovskite cathode, thermochemically reduced under a 5% H_2/N_2 atmosphere

at 850 $^\circ$C for a duration time of 2 h, is presented in Fig. S3(c). The exsolved particles depicted in the SEM image, with an approximate size of 60 nm and a sparse number density, may not have a substantial contribution to the conductivity of the electrode.

We would like to emphasize that the electrochemical switching explored in our study diverges from the activation process typically seen in SOFCs/SOECs that contain pre-deposited or pre-exsolved transition metal (such as nickel) nanoparticles, for reasons. Firstly, electrochemical exsolution can be accomplished within mere minutes, a stark contrast to the thermochemical exsolution process which requires several hours, followed by an activation process. Secondly, as the cell voltage increases to the electrochemical switching point, the LSCF cathode undergoes deactivation due to the reduction of the LSCF cathode (and the decrease in the density of the charge carriers) and the consequent decrease in its electrical conductivity caused by cathodic polarization. Thirdly, the change in instantaneous resistance at the electrochemical switching point is much more pronounced compared to the activation process. As depicted in Fig. S4, which corresponds to Fig. 5(a), the instantaneous resistance goes up to 1477 Ω cm^2 at –0.85 V, then diminishes to 1.7 Ω cm^2 at –2 V. This substantial fluctuation in instantaneous resistance is a unique characteristic that sets the electrochemical exsolution and switching apart from the activation process described in the literature [30].

The effect of temperature on the electrochemical behavior of the LSCF cell was examined over a temperature range of 700 $^\circ$C to 850 $^\circ$C during electrolysis. Fig. 6(a) depicts the relationship between current density and cell voltage at different temperatures, using a scan rate of 1 mV s^{-1}. Notably, higher temperatures corresponded to elevated current densities due to the enhanced electrolysis of H_2O and CO_2. To focus on a specific voltage range following a flat region, a zoomed graph in the inset of Fig. 6(a) is presented, capturing the initial take-off point. Interestingly, the take-off cell voltage demonstrated a decrease with increasing temperature. This trend is also evident in the ASR graph presented in Fig. 6(b). As temperature increased, ASRs exhibited a decline, while the electrochemical switching points occurred at lower cell voltages. This behavior can be attributed to the formation of exsolved metal nanoparticles. As the temperature rises, the rate of thermochemical oxidation of metal nanoparticles and LSCF perovskite by gas phase oxidants, H_2O and CO_2, accelerates. Simultaneously, the electrochemical reduction of LSCF and the exsolution of metal nanoparticles by supplied electrons also occur at a faster rate due to the reduced resistance. Consequently, the shift to lower voltage in the electrochemical switching point with increasing temperature suggests that the impact of temperature on enhancing the electrochemical reduction outweighs its effect on promoting thermochemical oxidation.
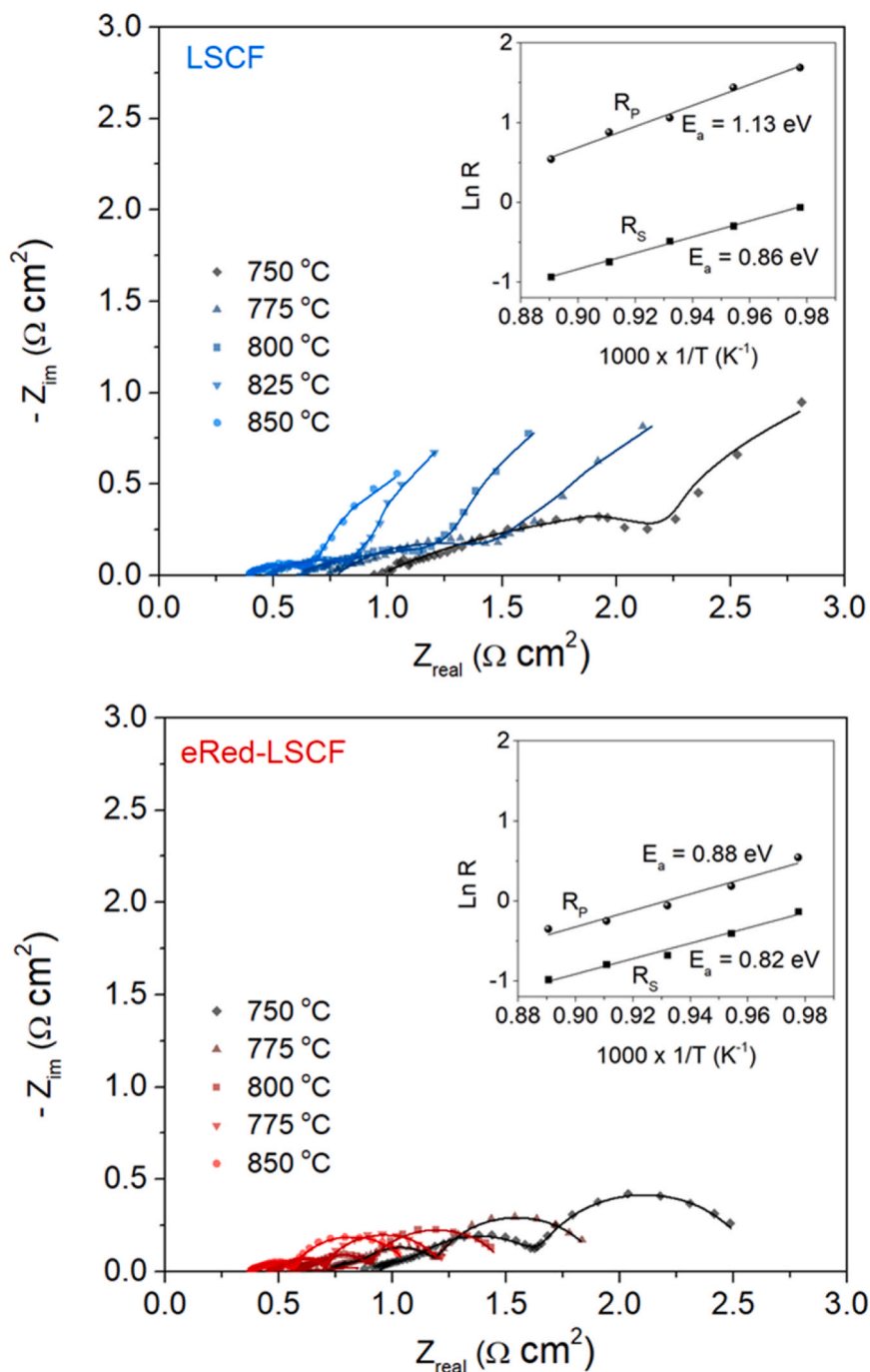
Fig. 8. Electrochemical impedance spectra of LSCF and eRed-LSCF for co-electrolysis of H_2O and CO_2 at different temperatures and Arrhenius plots of R_P and R_S.

Fig. 6(c) presents Arrhenius plots illustrating the activation energy for SOECs at various cell voltages. The calculated activation energies for ASRs at –0.5 V and –0.75 V, which lie before the electrochemical switching point, were found to be 0.35 eV and 0.34 eV, respectively. The similar activation energy values across the increasing cell voltage range suggest that gas diffusion and the adsorption of gas-phase oxidants are the primary factors influencing the ASRs at these voltage levels, where electrochemical switching has not yet occurred. However, at –1.25 V, the activation energy for ASRs notably increased to 1.13 eV. Subsequently, the activation energy values gradually decreased with further increases in cell voltage, measuring 0.82 eV at –1.50 V, 0.66 eV at –1.75 V, and 0.57 eV at –2.00 V. It should be noted that charge transfer resistance is a thermal activation process, whereas gas diffusion and adsorption are predominantly pressure-dependent, rather than being influenced by temperature [31,32]. This implies that at lower voltages with low activation energy, gas diffusion and adsorption may represent the primary barriers to the electrolysis of H_2O and CO_2. The activation energy of 1.13 eV observed at a cell voltage of –1.25 V, the highest among the ASRs, can be attributed to the presence of electrochemically reduced LSCF surfaces containing metal nanoparticles, which improve the adsorption of gas-phase oxidants and enhance the electrical conductivity of the electrode. Given the high activation energy (1.13 eV) observed at the –1.25 V cell voltage, it can be inferred that the primary barrier to electrolysis is the charge transfer. However, further reduction of the LSCF electrode at higher cell voltages and the resulting exsolution of metal nanoparticles provide metallic conductivity at higher cell
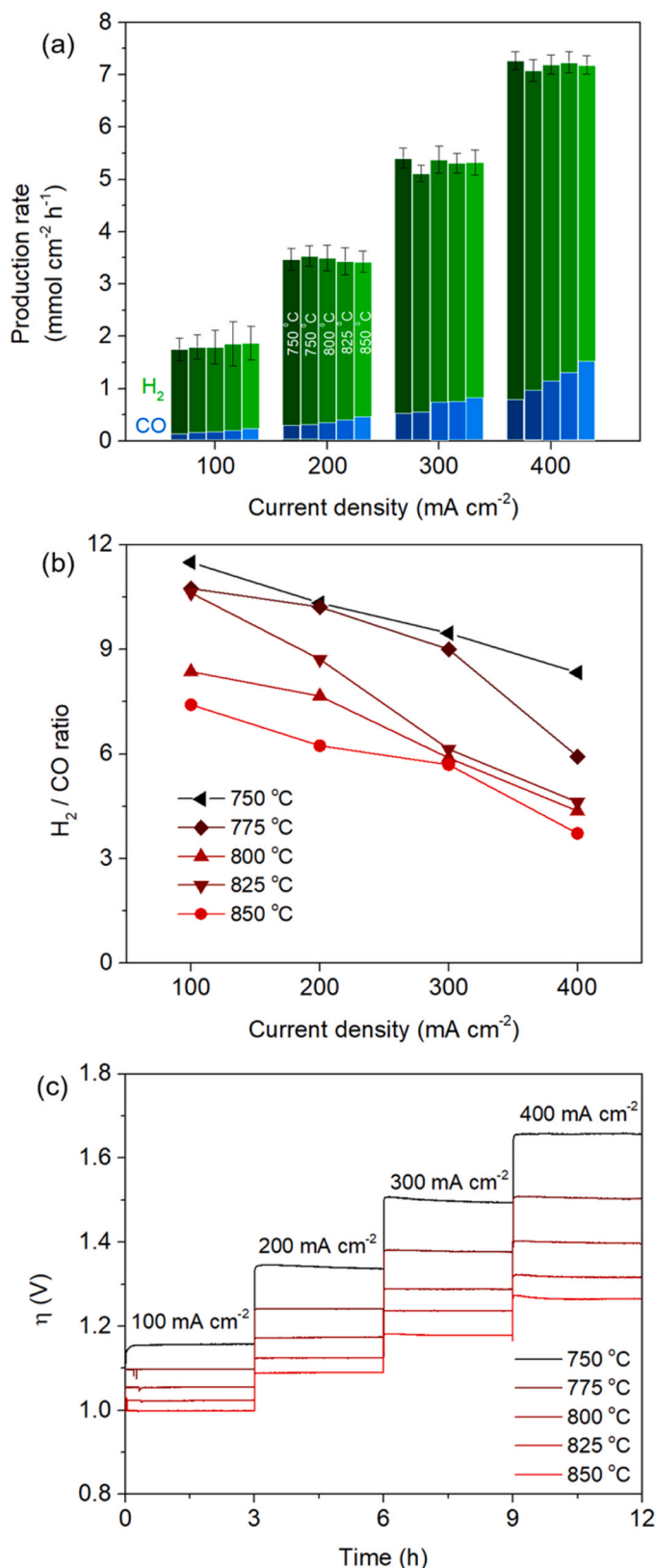
Fig. 9. (a) Production rates of H_2 and CO and (b) the ratio of H_2 to CO, (c) the cell overpotential for co-electrolysis of H_2O and CO_2 on eRed-LSCF.

voltages, thereby causing a decrease in activation energy.

3.4. Electrolysis of H_2O and CO_2

The electrocatalytic performance of LSCF and electrochemically reduced LSCF (eRed-LSCF) for the electrolysis of H_2O, CO_2, and H_2O/CO_2 was investigated by comparing Nyquist plots under open circuit voltage. The resulting polarization resistances (R_P) were also determined. eRed-LSCF was prepared by applying –2 V of cathodic polarization for 2 min at 850 °C. It should be noted that 850 °C represents the maximum electrolysis temperature utilized in this study and extending the duration beyond 2 min did not yield any further improvements in resistance. The exsolved particles on eRed-LSCF, as illustrated in Fig. S5, exhibit approximately 300 nm of size and remarkably high number density. Fig. 7(a) presents Nyquist plots obtained under open circuit voltage for the electrolysis of H_2O, CO_2, and H_2O/CO_2 on both LSCF and eRed-LSCF electrodes. The impedance spectra were fitted with three different resistances, including the ohmic resistance (R_S) and the polarization resistance (R_P). The R_S value, which corresponds to the high-frequency intercepts, did not show significant difference for all three reactions and regardless of the LSCF cathode reduction. This value can be attributed to factors such as the electrolyte thickness, contact resistances, and the resistances of current collectors and contacts [33]. The R_P, calculated by fitting the impedance spectra using the equivalent circuit in Fig. 7(b), displayed a 76–78% decrease on the eRed-LSCF cell compared to the LSCF cell, indicating a lower electric energy requirement for H_2O, H_2O/CO_2, and CO_2 electrolysis.

Fig. 8 illustrates the impedance spectra on the LSCF and eRed-LSCF cells for co-electrolysis of H_2O and CO_2 at different temperatures, showing a decrease in both R_S and R_P with increasing temperature. The values of R_S were similar for both cells, resulting in an activation energy of 0.86 eV for LSCF and 0.88 eV for eRed-LSCF, as depicted in the inset figures. This activation energy can be attributed to O^{2-} ion conduction through the yttria-stabilized zirconia (YSZ) electrolyte and typically falls within the range of 0.7–1.4 eV [34]. Furthermore, the eRed-LSCF cell demonstrated significantly improved performance compared to the LSCF cell. It exhibited a lower R_P with an estimated activation energy of 0.88 eV, which corresponds to a 22% reduction compared to the R_P of 1.13 eV observed in the LSCF cell. This enhanced electrocatalytic performance in the eRed-LSCF cell can be attributed to improved adsorption properties for H_2O and CO_2, as well as reduced oxidation states of B-site transition metals facilitated by exsolved nanoparticles and abundant oxygen vacancies. The reduction of LSCF electrode, through either electrochemical or thermochemical means, induces the formation of oxygen vacancies as shown in Eqs. 1 and 2. These vacancies serve as active adsorption sites for both H_2O and CO_2. Fig. S6 provides further insights into the improved surface adsorption of H_2O and CO_2 on thermochemically reduced LSCF using Temperature-programmed desorption-Diffuse reflectance infrared Fourier Transform spectroscopy (TPD-DRIFTS).

The normalized production rate of H_2 and CO during the co-electrolysis of H_2O and CO_2 on the eRed-LSCF cell at different temperatures and current densities is presented in Fig. 9(a). The Faradaic efficiency consistently was above 93% for all temperatures and current densities, indicating the exceptional efficiency of the eRed-LSCF cell. Such high Faradaic efficiency, which is a distinguishing characteristic of high-temperature solid oxide electrolysis cells (SOECs), verifies the minimized electron consumption for carbon formation on the cathode surface. The formation of carbon during CO_2 electrolysis can significantly impede cathode performance by obstructing active sites [35]. Interestingly, despite the equimolar supply of H_2O and CO_2, H_2O electrolysis predominated over CO_2 electrolysis due to the slower kinetics associated with CO_2 electrolysis [36]. It has been reported that reverse water-gas shift reaction (r-WGS) could be responsible for the production of CO during co-electrolysis of H_2O/CO_2 [36,37]. It has been reported that the extent of r-WGS reaction during co-electrolysis of H_2O/CO_2

depends on operating temperature, gas composition, applied current, and voltage [38,39]. Fig. 9(b) illustrates the significant influence of temperature and current density on the H_2/CO ratio during the co-electrolysis of H_2O and CO_2. The slower kinetics of CO_2 electrolysis contribute to a higher H_2/CO ratio at lower temperatures, while r-WGS reactions tend to occur at higher temperatures, resulting in increased CO production. Additionally, a higher current density intensifies H_2 production in the reaction environment, thereby reducing the H_2/CO ratio. Lastly, Fig. 9(c) demonstrates the stability of the eRed-LSCF cell over a 3 h period during co-electrolysis, showing no noticeable increase in voltage. This indicates the excellent stability of the eRed-LSCF cell under prolonged operating conditions, even without a safety gas. Although the absence of a safety gas enhances the efficiency of electrolysis, the necessity of a safety gas to maintain a reduced state of transition metals in the state-art electrodes, such as Ni/YSZ, remains a subject of debate [28, 40–42]. However, the findings in this study suggest that the use of a safety gas is unnecessary. Other studies have reported the stability of perovskite electrodes, both with and without nanoparticles, during electrolysis without the co-feeding of a safety gas [35,43,44].

4. Conclusions

This study provides a comprehensive understanding of the electro-chemical behavior during electrolysis by investigating the electro-chemical reduction of LSCF perovskite and the subsequent exsolution of metal nanoparticles. By applying cathodic polarization for a short duration, successful electrochemical reduction of LSCF perovskite and exsolution of metal nanoparticles were achieved, as confirmed by microscopic images displaying the exsolution of metal nanoparticles. *Operando* X-ray absorption near-edge structure analysis conducted during electrolysis demonstrated a significant reduction in the oxidation state of B-site atoms, particularly cobalt, within the LSCF electrode. The electrochemical behavior of the LSCF electrode during electrolysis exhibited dynamic changes in current density and area-specific resistance in response to variations in cell voltage, attributable to instantaneous alterations in electrical conductivity and surface adsorption properties. The electrochemical switching point, marked by the transition from an increasing trend to a decreasing trend in area-specific resistance, was identified. Remarkably, the eRed-LSCF electrode displayed excellent stability and significantly lowered polarization resistance during the electrolysis of H_2O and/or CO_2, without the requirement of a safety gas.

CRediT authorship contribution statement

Jaesung Kim: Conceptualization, Investigation, Methodology, Data curation, Formal analysis, Writing - original draft. **Seval Gunduz:** Investigation, Formal analysis, Writing - review & editing. **Anne C. Co:** Formal analysis, Writing - review. **Umit S. Ozkan:** Conceptualization, Funding acquisition, Project administration, Resources, Supervision, Formal analysis, Writing - review & editing.

Declaration of Competing Interest

The authors declare that they have no known competing financial interests or personal relationships that could have appeared to influence the work reported in this paper.

Data availability

Data will be made available on request.

Acknowledgements

Appendix A. Supporting information

Supplementary data associated with this article can be found in the online version at doi:10.1016/j.apcatb.2023.123603.

References

[1] R.R. Hudgins, P.L. Silveston, C.-Y. Li, A.A. Adesina, Partial Oxidation and Dehydrogenation of Hydrocarbons. Periodic Operation of Chemical Reactors, Elsevier,, 2013, pp. 79–122.

[2] R. Watanabe, Y. Hondo, K. Mukawa, C. Fukuhara, E. Kikuchi, Y. Sekine, Stable and selective perovskite catalyst for dehydrogenation of propane working with redox mechanism, J. Mol. Catal. A Chem. 377 (2013) 74–84, https://doi.org/10.1016/j.molcata.2013.04.033.

[3] S. Royer, D. Duprez, F. Can, X. Courtois, C. Batiot-Dupeyrat, S. Laassiri, H. Alamdari, Perovskites as substitutes of noble metals for heterogeneous catalysis: dream or reality, Chem. Rev. 114 (2014) 10292–10368, https://doi.org/10.1021/cr500032a.

[4] K. Chen, E. Iglesia, A.T. Bell, Isotopic tracer studies of reaction pathways for propane oxidative dehydrogenation on molybdenum oxide catalysts, J. Phys. Chem. B 105 (2001) 646–653, https://doi.org/10.1021/jp002100x.

[5] K. Huang, An emerging platform for electrocatalysis: perovskite exsolution, Sci. Bull. 61 (2016) 1783–1784, https://doi.org/10.1007/s11434-016-1194-8.

[6] D. Neagu, V. Kyriakou, I.L. Roiban, M. Aouine, C. Tang, A. Caravaca, K. Kousi, I. Schreur-Piet, I.S. Metcalfe, P. Vernoux, M.C.M. van de Sanden, M.N. Tsampas, In situ observation of nanoparticle exsolution from perovskite oxides: from atomic scale mechanistic insight to nanostructure tailoring, ACS Nano 13 (2019) 12996–13005, https://doi.org/10.1021/acsnano.9b05652.

[7] D. Neagu, G. Tsekouras, D.N. Miller, H. Menard, J.T. Irvine, In situ growth of nanoparticles through control of non-stoichiometry, Nat. Chem. 5 (2013) 916–923, https://doi.org/10.1038/nchem.1773.

[8] Y. Sun, J. Li, Y. Zeng, B.S. Amirkhiz, M. Wang, Y. Behnamian, J. Luo, A-site deficient perovskite: the parent for in situ exsolution of highly active, regenerable nano-particles as SOFC anodes, J. Mater. Chem. A 3 (2015) 11048–11056, https://doi.org/10.1039/C5TA01733E.

[9] S.-K. Otto, K. Kousi, D. Neagu, L. Bekris, J. Janek, I.S. Metcalfe, Exsolved nickel nanoparticles acting as oxygen storage reservoirs and active sites for redox CH_4 conversion, ACS Appl. Ener. Mater. 2 (2019) 7288–7298, https://doi.org/10.1021/acsaem.9b01267.

[10] S. Joo, O. Kwon, K. Kim, S. Kim, H. Kim, J. Shin, H.Y. Jeong, S. Sengodan, J. W. Han, G. Kim, Cation-swapped homogeneous nanoparticles in perovskite oxides for high power density, Nat. Commun. 10 (2019) 697, https://doi.org/10.1038/s41467-019-08624-0.

[11] Y.R. Jo, B. Koo, M.J. Seo, J.K. Kim, S. Lee, K. Kim, J.W. Han, W. Jung, B.J. Kim, Growth Kinetics of Individual Co Particles Ex-solved on $SrTi_{0.75}Co_{0.25}O_{3-\delta}$ Polycrystalline Perovskite Thin Films, J. Am. Chem. Soc. 141 (2019) 6690–6697, https://doi.org/10.1021/jacs.9b01882.

[12] B. Hua, M. Li, Y.F. Sun, J.H. Li, J.L. Luo, Enhancing perovskite electrocatalysis of solid oxide cells through controlled exsolution of nanoparticles, ChemSusChem 10 (2017) 3333–3341, https://doi.org/10.1002/cssc.201700936.

[13] J.G. Lee, J.H. Myung, A.B. Naden, O.S. Jeon, Y.G. Shul, J.T.S. Irvine, Replacement of Ca by Ni in a Perovskite Titanate to Yield a Novel Perovskite Exsolution Architecture for Oxygen-Evolution Reactions, Adv. Ener. Mat. 10 (2020), https://doi.org/10.1002/aenm.201903693.

[14] D. Neagu, T.S. Oh, D.N. Miller, H. Menard, S.M. Bukhari, S.R. Gamble, R.J. Gorte, J.M. Vohs, J.T.S. Irvine, Nano-socketed nickel particles with enhanced coking resistance grown in situ by redox exsolution, Nat. Commun. 6 (2015) 8120, https://doi.org/10.17630/2CA88024-4A83-4690-B66F-BA3B98A052D1.

[15] S.P. Jiang, Nanoscale and nano-structured electrodes of solid oxide fuel cells by infiltration: Advances and challenges, Inter. J. Hydrog. Ener. 37 (2012) 449–470, https://doi.org/10.1016/j.ijhydene.2011.09.067.

[16] S. Kim, A. Jun, O. Kwon, J. Kim, S. Yoo, H.Y. Jeong, J. Shin, G. Kim, Nanostructured double perovskite cathode with low sintering temperature for intermediate temperature solid oxide fuel cells, ChemSusChem 8 (2015) 3153–3158, https://doi.org/10.1002/cssc.201500509.

[17] D.J. Deka, J. Kim, S. Gunduz, M. Aouine, J.-MM. Millet, A.C. Co, U.S. Ozkan, Investigation of hetero-phases grown via in-situ exsolution on a Ni-doped (La,Sr) FeO_3 cathode and the resultant activity enhancement in CO_2 reduction, Appl. Catal. B: Environ. 286 (2021), https://doi.org/10.1016/j.apcatb.2021.119917.

[18] W. Fan, B. Wang, R. Gao, G. Dimitrakopoulos, J. Wang, X. Xiao, L. Ma, K. Wu, B. Yildiz, J. Li, Anodic shock-triggered exsolution of metal nanoparticles from

perovskite oxide, J. Am. Chem. Soc. 144 (2022) 7657–7666, https://doi.org/10.1021/jacs.1c12970.

[19] J.H. Myung, D. Neagu, D.N. Miller, J.T. Irvine, Switching on electrocatalytic activity in solid oxide cells, Nat 537 (2016) 528–531, https://doi.org/10.17630/c93efdb1-65a9-4f39-9277-2f56580d3b77.

[20] A.K. Opitz, A. Nenning, V. Vonk, S. Volkov, F. Bertram, H. Summerer, S. Schwarz, A. Steiger-Thirsfeld, J. Bernardi, A. Stierle, J. Fleig, Understanding electrochemical switchability of perovskite-type exsolution catalysts, Nat. Commun. 11 (2020) 4801, https://doi.org/10.1038/s41467-021-25320-0.

[21] H. Lv, T. Liu, X. Zhang, Y. Song, H. Matsumoto, N. Ta, C. Zeng, G. Wang, X. Bao, Atomic-Scale Insight into Exsolution of CoFe Alloy Nanoparticles in $La_{0.4}Sr_{0.6}Co_{0.2}Fe_{0.7}Mo_{0.1}O_{3-\delta}$ with Efficient CO_2 Electrolysis, Angew. Chem. Int. Ed. Engl. 59 (2020) 15968–15973, https://doi.org/10.1002/anie.202006536.

[22] D.J. Deka, S. Gunduz, T. Fitzgerald, J.T. Miller, A.C. Co, U.S. Ozkan, Production of syngas with controllable H_2/CO ratio by high temperature co-electrolysis of CO_2 and H_2O over Ni and Co- doped lanthanum strontium ferrite perovskite cathodes, Appl. Catal. B: Environ. 248 (2019) 487–503, https://doi.org/10.1016/j.apcatb.2019.02.045.

[23] A. Vaitkus, A. Merkys, S. Grazulis, Validation of the crystallography open database using the crystallographic information framework, J. Appl. Crystallogr. 54 (2021) 661–672, https://doi.org/10.1107/S1600576720016532.

[24] B.H. Toby, R.B. Von Dreele, GSAS-II: the genesis of a modern open-source all purpose crystallography software package, J. Appl. Crystallogr. 46 (2013) 544–549, https://doi.org/10.1107/S0021889813003531.

[25] S. Gunduz, D.J. Deka, J. Kim, M. Wilson, M. Warren, U.S. Ozkan, Incident-angle dependent operando XAS cell design: investigation of the electrochemical cells under operating conditions at various incidence angles, RSC Adv. 11 (2021) 6456–6463, https://doi.org/10.1039/D0RA09579F.

[26] B. Ravel, M. Newville, ATHENA, ARTEMIS, HEPHAESTUS: data analysis for X-ray absorption spectroscopy using IFEFFIT, J. Synchrotron Radiat. 12 (2005) 537–541, https://doi.org/10.1107/S0909049505012719.

[27] J. Kim, Y.J. Kim, M. Ferree, S. Gunduz, A.C. Co, M. Kim, U.S. Ozkan, In-situ exsolution of bimetallic CoFe nanoparticles on (La,Sr)FeO_3 perovskite: Its effect on electrocatalytic oxidative coupling of methane, Appl. Catal. B: Environ. 321 (2023), https://doi.org/10.1016/j.apcatb.2022.122026.

[28] Y. Song, Z. Zhou, X. Zhang, Y. Zhou, H. Gong, H. Lv, Q. Liu, G. Wang, X. Bao, Pure CO_2 electrolysis over an Ni/YSZ cathode in a solid oxide electrolysis cell, J. Mater. Chem. A 6 (2018) 13661–13667, https://doi.org/10.1039/C8TA02858C.

[29] K. Ikeda, Electrical Resistivity of Nickel, Cobalt, and Their Alloys, Trans. Jpn. Inst. Met. 29 (1988) 183–190, https://doi.org/10.2320/matertrans1960.29.183.

[30] N. Duan, M. Gao, B. Hua, M. Li, B. Chi, J. Li, J.-L. Luo, Exploring $Ni(Mn_{1/3}Cr_{2/3})_2O_4$ spinel-based electrodes for solid oxide cells, J. Mater. Chem. A 8 (2020) 3988–3998, https://doi.org/10.1039/C9TA11878K.

[31] Y. Chen, S. Yoo, Y. Choi, J.H. Kim, Y. Ding, K. Pei, R. Murphy, Y. Zhang, B. Zhao, W. Zhang, H. Chen, Y. Chen, W. Yuan, C. Yang, M. Liu, A highly active, CO_2-tolerant electrode for the oxygen reduction reaction, Ener. Environ. Sci. 11 (2018) 2458–2466, https://doi.org/10.1039/C8EE01140K.

[32] Y. Chen, Y. Choi, S. Yoo, Y. Ding, R. Yan, K. Pei, C. Qu, L. Zhang, I. Chang, B. Zhao, Y. Zhang, H. Chen, Y. Chen, C. Yang, B. deGlee, R. Murphy, J. Liu, M. Liu, A Highly

Efficient Multi-phase Catalyst Dramatically Enhances the Rate of Oxygen Reduction, Joule 2 (2018) 938–949, https://doi.org/10.1016/j.joule.2018.02.008.

[33] E. Hernández, F. Baiutti, A. Morata, M. Torrell, A. Tarancón, Infiltrated mesoporous oxygen electrodes for high temperature co-electrolysis of H_2O and CO_2 in solid oxide electrolysis cells, J. Mater. Chem. A 6 (2018) 9699–9707, https://doi.org/10.1039/C8TA01045E.

[34] B. Shri Prakash, S. Senthil Kumar, S.T. Aruna, Effect of composition on the polarization and ohmic resistances of LSM/YSZ composite cathodes in solid oxide fuel cell, Bull. Mater. Sci. 40 (2017) 441–452, https://doi.org/10.1007/s12034-017-1401-5.

[35] M. Torrell, S. Garcia-Rodriguez, A. Morata, G. Penelas, A. Tarancon, Co-electrolysis of steam and CO_2 in full-ceramic symmetrical SOECs: a strategy for avoiding the use of hydrogen as a safe gas, Faraday Discuss. 182 (2015) 241–255, https://doi.org/10.1039/C5FD00018A.

[36] S.-W. Kim, M. Park, H. Kim, K.J. Yoon, J.-W. Son, J.-H. Lee, B.-K. Kim, J.-H. Lee, J. Hong, In-situ nano-alloying Pd-Ni for economical control of syngas production from high-temperature thermo-electrochemical reduction of steam/CO_2, Appl. Catal. B: Environ. 200 (2017) 265–273, https://doi.org/10.1016/j.apcatb.2016.07.008.

[37] F. Alenazey, Y. Alyousef, O. Almisned, G. Almutairi, M. Ghouse, D. Montinaro, F. Ghigliazza, Production of synthesis gas (H_2 and CO) by high-temperature Co-electrolysis of H_2O and CO_2, Inter. J. Hydrog. Ener. 40 (2015) 10274–10280, https://doi.org/10.1016/j.ijhydene.2015.06.034.

[38] D.J. Deka, J. Kim, S. Gunduz, M. Ferree, A.C. Co, U.S. Ozkan, Temperature-induced changes in the synthesis gas composition in a high-temperature H_2O and CO_2 co-electrolysis system, Appl. Catal. A Gener. 602 (2020), https://doi.org/10.1016/j.apcata.2020.117697.

[39] Y. Wang, T. Liu, L. Lei, F. Chen, High temperature solid oxide H_2O/CO_2 co-electrolysis for syngas production, Fuel Process. Technol. 161 (2017) 248–258, https://doi.org/10.1016/j.fuproc.2016.08.009.

[40] Q. Li, Y. Zheng, Y. Sun, T. Li, C. Xu, W. Wang, S.H. Chan, Understanding the occurrence of the individual CO_2 electrolysis during H_2O-CO_2 co-electrolysis in classic planar Ni-YSZ/YSZ/LSM-YSZ solid oxide cells, Electrochim. Acta 318 (2019) 440–448, https://doi.org/10.1016/j.electacta.2019.06.108.

[41] T. Wang, J. Wang, L. Yu, Z. Ye, X. Hu, G.E. Marnellos, D. Dong, Effect of NiO/YSZ cathode support pore structure on CO_2 electrolysis via solid oxide electrolysis cells, J. Eur. Ceram. Soc. 38 (2018) 5051–5057, https://doi.org/10.1016/j.jeurceramsoc.2018.07.005.

[42] H. Zheng, Y. Tian, L. Zhang, B. Chi, J. Pu, L. Jian, $La_{0.8}Sr_{0.2}Co_{0.8}Ni_{0.2}O_{3-\delta}$ impregnated oxygen electrode for H_2O/CO_2 co-electrolysis in solid oxide electrolysis cells, J. Power Sources 383 (2018) 93–101, https://doi.org/10.1016/j.jpowsour.2018.02.041.

[43] Y. Li, P. Li, B. Hu, C. Xia, A nanostructured ceramic fuel electrode for efficient CO_2/H_2O electrolysis without safe gas, J. Mater. Chem. A 4 (2016) 9236–9243, https://doi.org/10.1039/C6TA02830F.

[44] L. Bian, C. Duan, L. Wang, Z. Chen, Y. Hou, J. Peng, X. Song, S. An, R. O'Hayre, An all-oxide electrolysis cells for syngas production with tunable H_2/CO yield via co-electrolysis of H_2O and CO_2, J. Power Sources 482 (2021), https://doi.org/10.1016/j.jpowsour.2020.228887.